 doi:10.20944/preprints201804.0043.v1

Article

Automatic Monitoring System Based on IoT and Vision Technology

Ting-Rong Chang [1] and Liang-Hwei Lee [1, *]

[1] Department of Civil Engineering, National Kaohsiung University of Science and Technology, No. 415, Jiangong Rd., Sanmin Dist., Kaohsiung 80778, Taiwan; trong42@nkust.edu.tw

* Correspondence: lhlee@cc.kuas.edu.tw; Tel.: +886-7-381-4526.

Abstract:

Multi-view stereo (MVS) employs multi-point photography for image point positioning and three-dimensional reconstruction technology. Recently, this technology has been introduced into the monitoring of road slopes due to advances in photography and computing technology. In general, the various phases of post-image processing procedures are applied to various photographic data. In this study a novel, automated image-monitoring system is proposed to improve the ability of automatic processing. First, an Internet of things (IoT)-based digital photography system architecture was constructed to provide automatic control of camera photography and real-time transmission of image data. In addition, a visual SfM-MVS 3D reconstruction technique was used to develop related software and hardware interfaces based on the built-in Python computing framework of Photoscan Pro. The software integrates fully automatic photography, image transmission, monitoring of data processing and product release programs. The experimental results show that the system architecture can be applied to fully automatic three-dimensional monitoring of road slopes.

Keywords: Monitoring; SfM-MVS; photogrammetry, internet of things, M3C2.

 doi:10.20944/preprints201804.0043.v1

1. Introduction

Road slope monitoring is a technique that uses monitoring methods to acquire slope stability data to provide early warning of instability. The most common methods can be divided into two categories: monitoring of stress and monitoring of surface displacement. Usually, stress monitoring employs engineering methods to set up relevant monitoring equipment. Mechanical analysis obtains the force per unit area in the monitored area, which is used as the basis for judging its stability. Common monitoring equipment includes inclinometers, borehole extensometers, surface extensometers, piezometers, water-level observation wells, rain gauges, crackmeters and anchor load cells. Surface displacement monitoring analyzes differences in three-dimensional surface area over a specified period as a monitoring and early warning technology. In practice, it is essential to obtain more accurate 3D coordinates by arranging a set of control points around the monitoring area. Common monitoring equipment includes, but is not limited to: laser interferometers, electronic distance measuring (EDM) systems, automatic motorized total stations, global navigation satellite systems (GNSSs), terrestrial laser scanners and photogrammetric systems for 3D reconstruction [1].

In recent years, due to the demand for large-scale slope monitoring, surface displacement monitoring has been proposed and applied using GPS monitoring systems, terrestrial laser scanner technology and 3D reconstruction based on photogrammetry. These techniques can be used as a reference for monitoring and possible warnings by analyzing the displacement of monitored points and differences in the three-dimensional surface area [2]. A GPS monitoring system can set multiple antenna arrays on the monitored points to obtain a continuous feed of high-precision data. However, due to its high installation cost, current use is limited to slopes that present immediate hazards. Terrestrial laser scanner technology is effective in obtaining the three-dimensional surface of a monitored area to calculate differences. Currently, the automation is not perfect, and it is difficult to install for long term use on a monitored site, so its use has been limited to the analysis of three-dimensional data in separate periods. Photogrammetric technology is widely used to model and obtain 3D surface information due to the development of 'structure from motion & multi-view stereo' (SfM-MVS) [3]. As the algorithm requires a high level of precision, the control points and data-adjustment calculations are included in the calculation. This method has gradually been applied to the measurement and monitoring of road slopes [4,5] and is also referred to as 'vision photogrammetry'. The advantages of this technique for road-slope monitoring include automatic measurement using code targets (CTs) and high-precision 3D coordinates of monitored points through multiple overlapping shots. Dense point clouds are obtained through surface reconstruction to provide surface-difference analysis of the monitored area. Compared to current GPS or terrestrial laser-scanner monitoring technology, photogrammetry can provide cheaper three-dimensional surface-monitoring solutions. However, this technology is presently still limited by the lack of full automation of photography, image transmission, calculation and analysis. Therefore, it is used only for temporal three-dimensional data-difference analysis in manual inspections.

The current, well-established monitoring systems integrate various monitoring methods, complete automatic data interpretation (recording and analysis) as well as quantitative monitoring data, which detect a variety of physical changes that are unobservable by the naked eye, to provide both early warning of instability and follow-up analysis. To automate measurements, this study proposes an automatic monitoring architecture based on photogrammetry. This provides fully automatic photography, image transmission, calculation, three-dimensional data-difference analysis and an early warning mechanism. The main improvements to current systems are the introduction of photogrammetry and monitoring technology to automate image shooting at set intervals to obtain images of a monitored area, which replaces traditional manual shooting; using SfM-MVS as the calculation core and total least squares (TLS) as the free network adjustment calculation framework to dispense with the need to set traditional control points outside the monitoring area

Preprints (www.preprints.org) | NOT PEER-REVIEWED | Posted: 4 April 2018 doi:10.20944/preprints201804.0043.v1

that are not expected to change, which will allow automatic monitoring and effectively reduce the threshold of photogrammetry monitoring technology; and the design of a point-cloud computing process to display differences and allow surface analysis. The automatic photographic system is composed of a single board computer (SBC) with an Internet of things (IoT) architecture and a digital camera. The automatic-photography system provides automatic image capturing of a monitored area and image transmission. The computing architecture uses an SfM-MVS computing core with surface reconstruction technology, point-cloud-difference analysis, and big-data analysis to build this system, which is implemented in Python.

2. System configuration

The IoT-based visual monitoring system comprises three major modules: the IoT automatic photography module (IoT_APM), SfM-MVS photogrammetry monitoring (SfM-MVS_PM) and the error analysis module (EAM). The IoT_APM is a self-contained on-site camera for photography and uploading of images. It is a combination of IoT architecture and photographic equipment. SfM-MVS_PM is a fully automated measurement and computation architecture based on SfM-MVS photogrammetric technology. EAM is a data display and early warning method that combines error analysis with a database. Figure 1 shows the system's processing flow.

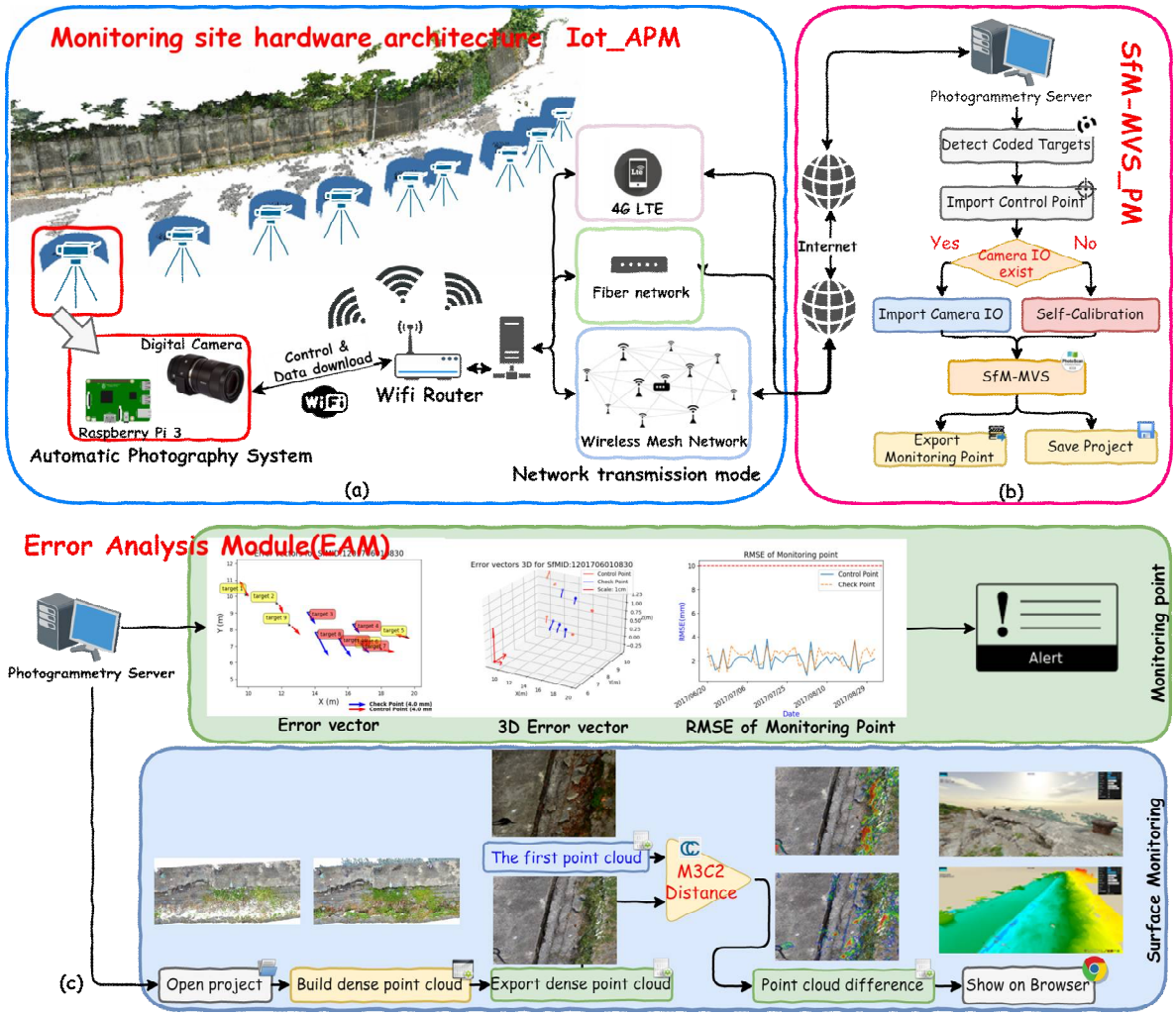

Figure 1. IoT vision monitoring system architecture

The IoT_APM erected at a surveillance site consists of several autonomous cameras. IoT communication and data transmission are provided using Wifi. The internet communication and data transmission can be provided using 4G LTE, a fiber network, or a wireless mesh network (Figure 1a). SfM-MVS_PM is a fully automated photogrammetric computing architecture. Figure 1b

Preprints (www.preprints.org) | NOT PEER-REVIEWED | Posted: 4 April 2018 doi:10.20944/preprints201804.0043.v1

shows the calculation process. The IoT_APM shoots images and sets up a project to open the automatic calculation program. Automatic measurement of monitored points is achieved by analyzing the locations of CTs, the control points in the monitored area, and the orientation parameters of each camera. The SfM-MVS method is used to calculate the three-dimensional data of the monitored points. Finally, the EAM, which can identify differences in the three-dimensional ground surface data between different periods, processes the data to provide early warning data. The calculation program calculates point-cloud differences between the dense point clouds of two periods in the form of M3C2 and transforms the results into the WebGL format as shown in Figure 1c.

2.1 Hardware architecture

The IoT_APM consists of multiple small single-board computers and digital cameras connected by IoT architecture. Each camera station in the automatic photography system is a combination of a Raspberry Pi 3 Model B, a set of PTZ servo motors and a digital camera. One camera is selected to be the main station with the function of shooting control and project establishment. Shooting control can be set up for single or scheduled shooting. A single shot is used to test the system and a repeat shot confirms the acquisition of data. Scheduled shooting is used to shoot at scheduled times. When the automatic photography has been completed, each camera station transfers its pictures to the server through FTP to perform automatic calculations. After the picture transfer has been completed, the master station creates a JSON project file for the server to enable automatic calculation of the task.

Various factors affect the photogrammetric accuracy, including camera resolution, camera focal length, and ground sample distance (GSD). This study chose a micro-monocular system that adjusts the camera distance or lens focal length according to the required monitoring accuracy. The camera can be controlled by the general-purpose input/output (GPIO) interface on the Raspberry Pi 3 Model B using a USB port integrated into the micro USB 15-pin connector (multi full micro USB) interface. This controls camera rotation, on/off, camera charging and data transmission. In addition, a camera with picture-transfer protocol (PTP) [6]/media-transfer protocol (MTP) [7] functions can be directly controlled by a micro-USB [8]. This function is defined in the USB 2.0 specification [9] and most current USB chips support USB port power control to control connection and disconnection of the camera function. However, in practice, products often lack the power-control circuit, preventing implementation of this function [10]. Therefore, if this method of control is considered, it must first be ascertained whether the device supports this feature. Figure 2a shows the analogous control of a Sony ILCE-QX1 camera. Figure 2b shows how to control a Sony ILCE-5100 using PTP digital control. In the following examples, we used PTP digital control as the hardware design.

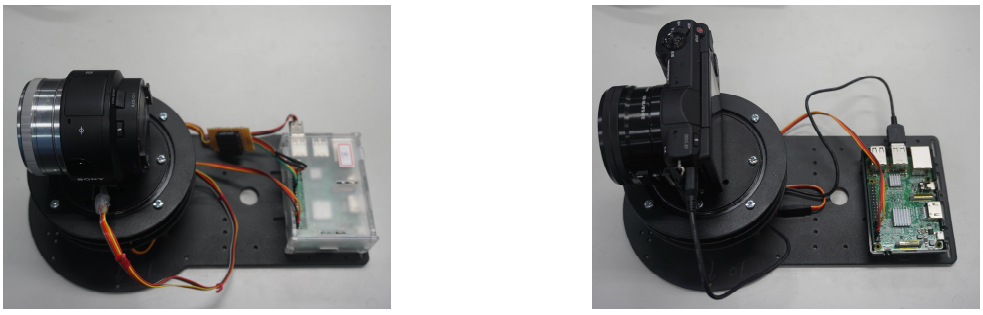

(a) (b)

Figure 2. Sony camera control: (a) analogy control and (b) PTP digital control.

2.2 Internet of things (IoT) architecture

In this architecture, IoT photography systems are usually connected to a LAN. Therefore, they require IP addresses to control and access related information via the socket or WebSocket and other communication protocols applied. In our system, the MQTT protocol is applied using an

Preprints (www.preprints.org) | NOT PEER-REVIEWED | Posted: 4 April 2018 doi:10.20944/preprints201804.0043.v1

IoT_APM because this protocol can send commands and deliver messages across the domain. Network security can be accomplished by user login requirements and SSL/TLS encryption and preservation.

Based on its built-in settings (Figure 3a), the IoT_APM determines which of the cameras is the master station and which are slave stations. The master station issues shooting commands and produces project files while the slave stations execute the shooting commands to accomplish a task as shown in Figure 3b. All cameras request photogrammetry server communication setting parameters, such as FTP connection IP, account number, password and current host status.

After completing the above actions, the IoT_APM will enter 'waiting task' status, as shown in Figure 3c. A task can be published by the main station or the photogrammetry server according to the task requirements (when re-shooting is required), and shooting tasks are started individually by each camera. As each camera completes shooting it sends a task-completed message to the master station; when the master station has received task-completed messages from all of the slave stations it creates a task project file (Figure 3b) and uploads all images to the photogrammetry server. If the host waits too long, a timeout status is sent out, cancelling the current task, and another shooting task is begun, as shown in Figure 3d.

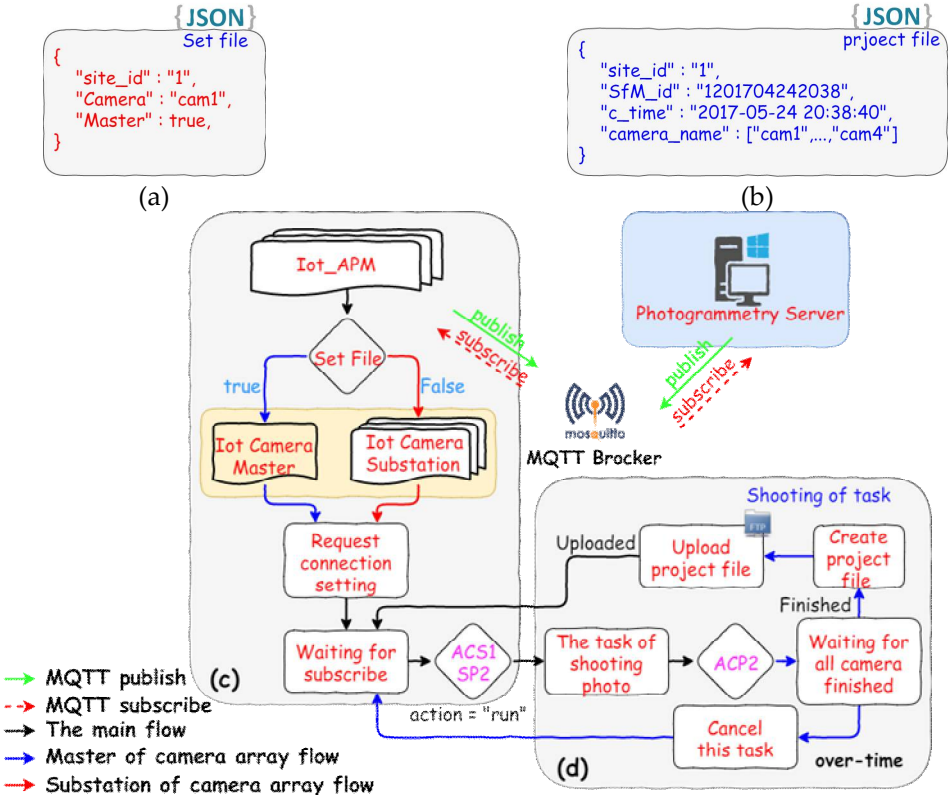

Figure 3. Network communication architecture of IoT_APM (a) Set file JSON format. (b) Project file JSON format. (c) Configuration of IoT_APM and (d) Iot_APM task of shooting photos.

Photographic measurements require the hardware to have a fixed focal length suitable for a given specific task, which is possible only by using a mechanical manual-focus lens. Autofocus mirrors can fix focal length only in internal focus mode. Although such lenses can be adjusted for manual focus when in the camera body, the focal length at each power-on process is subject to change due to lens inspection procedures. The price of a mechanical manual focusing lens is usually higher than autofocusing mirrors. Therefore, to minimize expense while deriving a fixed focal length this study proposes a procedure for an autofocusing lens to control the camera. First, the camera is adjusted to autofocus mode before shooting and focused on infinity. It is then locked and the focus is adjusted back to manual focus mode. The automatic photography and uploading process is shown in Figure 4a.

Preprints (www.preprints.org) | NOT PEER-REVIEWED | Posted: 4 April 2018 doi:10.20944/preprints201804.0043.v1

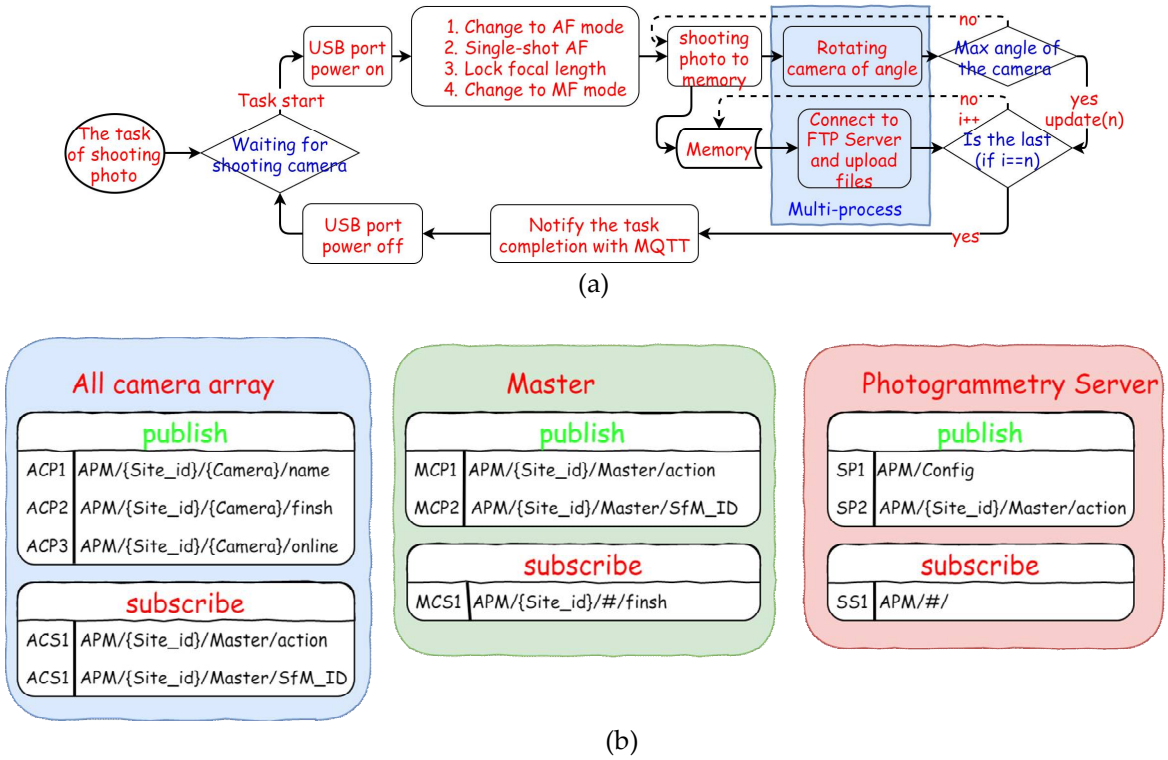

Figure 4. (a) Architecture of the task of IoT camera for shooting photographs. (b) MQTT topic of IoT_APS."{Site_id}" and "{Camera}" are variables, and the # wildcard symbol is used to subscribe for all levels.

To commence a task, the USB port control is powered on to turn on the PTP control cable and then the camera is focused, as above. The shooting and uploading procedures are carried out simultaneously. The shooting flow is driven by the servo motor, based on the shooting angle, and stored in the memory unit. FTP communication protocol is initiated to upload the photos sequentially. After completing shooting, a completion message is issued using MQTT and the USB port is powered off to disconnect the PTP control.

In the proposed architecture, the MQTT protocol provides the functionality of publishing and subscribing as shown in Figure 4b. The master can identify the number of hosts currently in the IoT camera array by subscribing to ACP1 through ACP3, as shown in Figure 4b. To start an automatic shooting task ACS1 and SP1, which are subscribed to by each camera, start shooting when the reply message is 'run'. After the task has been completed, each camera releases the task name using ACP2 and the master determines when all cameras have completed the task based on ACP2 subscription.

2.3 Automatic monitoring system of the data processor

This study developed an SfM-MVS_PM module based on the built-in Python environment of Agisoft PhotoScan Pro (1.3.3 64bit Windows OS). PhotoScan Pro provides SfM-MVS-related calculations. A point-cloud-difference calculation is performed using a CloudCompare M3C2 module, and remaining calculation functions are developed in Python. The system architecture supports multiple monitoring stations simultaneously; therefore, the system automatically executes the calculation program according to the project file system structure created by the IoT_APM. System folders can be divided into three parts: IoT_APM image upload and project file folders, photogrammetric automatic monitoring system calculations and analysis folders, and scheduling and point-cloud-difference analysis display-system folders.

The project file, written in JSON format, activates calculations by the photogrammetry server, which describes 'site_id', 'project_id', build time ('c_time') and all the camera numbers ('camera_folders') controlled by the site, as shown in the above Figure 3b. The photogrammetry

Preprints (www.preprints.org) | NOT PEER-REVIEWED | Posted: 4 April 2018 doi:10.20944/preprints201804.0043.v1

server scans the project folder continuously to enable automatic calculation tasks. The server also retrieves data from the database and file system based on the parameters stored in the project file to obtain the automatic calculation parameters.

Figure 5 shows the structure of the calculation folder, with the project file variables shown in red. The system root folder is named *'root'* and below this is the '*Images*' folder where the IoT_APM stores images. For the accuracy analysis module the *'cp'*, *'Camera'*, *'pj'*, and *'RMSE'* folders store control point data, camera calibration parameters, project file, and root mean square error (RMSE) analysis results, respectively. The *'cp'* folder contains measured 3D data (XML-format control point data) obtained from the monitored ground field using the file-naming rule, '*site_id+cp.xml*', for the purpose of subsequent automatic reading. The *'Camera'* folder uses site_id and the naming rule '*camera_site_id.xml*' to identify monitored areas and holds the calibration parameters. The *'point'* folder stores the analysis of point-cloud data and the *'C2C'* folder holds differences between pairs of point-cloud files. Finally, the WebGL-based point-cloud files are saved in the *'potree'* folder.

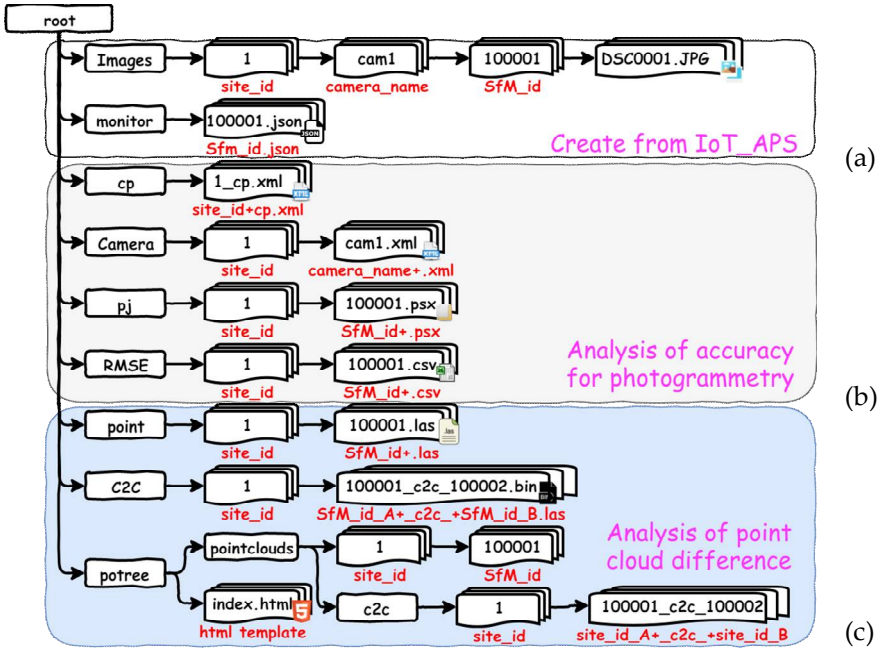

Figure 5. Folder architecture of photogrammetric automatic monitoring system (a) IoT_APS uploaded images and the project file created (b) Photogrammetric automatic monitoring system for automatic calculation and analysis and (c) display and analysis of point-cloud differences.

This system uses a database to record and control all automated processes. Table *'site'* is the core table that is used to manage monitoring station information, including latitude and longitude and other details of the site. The table *'account'* is used to store contact information for each monitoring station administrator, for internal notifications. The associated table *'site'* contains 'iot' and 'sfm' for recording whether a site contains an IoT_APS, and each calculation project. The table *'sfm'* is used to record the project creation of the close-range photogrammetric monitoring system, error-analysis information and the 3D coordinates of monitored points from the related table *'gcp'*. The related data sheet for 'sfm' also contains 'tasks' and 'c2c', which describe scheduled tasks and point-cloud differences in table *'sfm'*. The 'c2cpotree' information in table *'c2c'* is used to record a list of Potree formats after analyzing point-cloud differences.

The cluster computing architecture uses the regional network to connect the photogrammetry server, three cluster nodes and a NAS data-storage system in tandem. Multi-server supports cluster-node task calculations and can be applied to other photogrammetric analyses. Other related servers include storage systems (FTP server, SQL server) and the IoT data exchange agreement (MQTT). In total, this architecture uses four workstations and one NAS system. One workstation operates the photogrammetry server and PostgreSQL; the NAS operates Mosquitto (MQTT broker),

Preprints (www.preprints.org) | NOT PEER-REVIEWED | Posted: 4 April 2018 doi:10.20944/preprints201804.0043.v1

an FTP server and the Network File System (NFS); and the remaining workstations operate as a clustering node. For fast system operation the Internet is bidirectional at 100 Mbps/s, and the intranet is 1 GbE/s.

3. Image data processing

To facilitate operation of the proposed monitoring system, automated photogrammetric technology is applied to the core function. The image-data-processing procedures include visual-positioning technology, photography, automatic measurement techniques, and analysis of monitoring data. The following sections outline the details of the methodology.

3.1 Vision-based 3D point positioning

3.1.1 SfM-MVS

Computer vision is based on the stereovision theory of projective geometry to represent the relative geometry of machines and spaces. Based on the development of the technology of structure from motion (SfM) [11], the 3D geometry of objects' positions in a sequence of images is described by the theories of multi-view stereo (MVS) [12] and 3D reconstruction in computer vision. In recent years, SfM-MVS 3D reconstruction technology combined with SfM and MVS has achieved a breakthrough. Dense-point-cloud technology based on the patch-based multi-view stereo (PMVS) algorithm [13] obtains three-dimensional surface information. A surface reconstruction technique completes the surface reconstruction of the 3D model using Poisson surface reconstruction [14] and texture mapping. At present, the complete set of technologies is called SfM-MVS or visual photogrammetry, and this technique is widely used in three-dimensional reconstruction, UAV imaging, and true ortho photogrammetry. Many virtual reality modeling and cartography software programs have recently become available commercially, such as the Bentley® ContextCapture Center, which currently includes only relatively simple measurement tools. Measurement-oriented software, such as AgiSoft® PhotoScan Pro and Pix4D®, is widely used in UAV image mapping, 3D geology, and archeology. The measurement accuracy of software is related to ground sample distance (GSD) and depending on shooting quality and appropriate control can be up to 0.5 pix [15,16].

3.1.2 Camera calibration

Camera calibration parameters are used to calibrate lens distortion, which plays a key role in photogrammetry, especially for non-measurement cameras, and numerous camera calibration methods have been developed. In general, these methods can be divided into two major categories based on whether a target is used: target or target-free. The former require the camera to be calibrated beforehand by photographing the targets to derive a collinear conditional solution [17]. The latter use images of a scene directly to measure conjugate points to derive the calibration parameters, a method termed self-calibration [18], which is often used in SfM-MVS. Camera calibration technology is well established and any existing software or tool can be used to obtain camera parameters either by self-calibration or by default, with particular attention paid to the algorithms used for the selected software tools. For example, SfM-MVS uses the camera model to describe the in-camera orientation parameters, measured in pixels. Photogrammetry uses the collinear condition to describe both the inner and outer orientation parameters in length (μm). The two camera distortion parameters compared here have the same symbol, however, the formulas for these symbols are completely different. Therefore, special attention must be paid when using these formulas.

3.1.3 Coded targets

Measurement automation based on CTs has been developed over the last five years. Two main types have been developed: concentric rings [19] (Figure 6a) and dot distributions [20] (Figure 6b),

Preprints (www.preprints.org) | NOT PEER-REVIEWED | Posted: 4 April 2018 doi:10.20944/preprints201804.0043.v1

which display simple and stable recognition and decoding performance, as confirmed by Hattori et al [21]. This study employs concentric rings of CTs.

(a) (b)

Figure 6. An example of the two types of CTs: (a) Dot distributions (b) Concentric rings.

In summary, the center point of a 12-bit target must cover a minimum of 9-10 pix and have a vertical shooting tilt angle of less than 50 degrees on the image. For instance, for a photogrammetric survey with a defined GSD of 1 cm, the center point of the target should be around 10 cm minimum (10 × GSD). As the global diameter of the target is 3.5 times the diameter of the center point, the whole target should have a minimum size of 35 cm (35 × GSD).

3.2 Data capture & preparation

1. Image capture mode

SfM-MVS shooting mode can be relaxed to cover the principle of high overlap shooting. Shooting is best in a vertical scene but shooting at multiple angles can increase the overall geometry [15]. Taking road slope monitoring as an example, the recording mode can be taken in parallel with Figure 7a or Figure 7b. If the automatic photography function is considered, shooting can take place on the street or from telegraph poles using multi-station rotary photography.

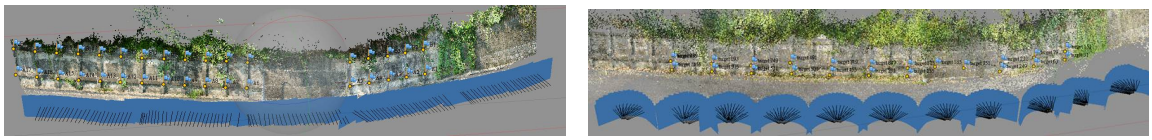

(a) (b)

Figure 7. SfM-MVS photogrammetry in roadside slope photography mode. (a) Parallel scene photography. (b) Multi-station rotation photography.

2. Monitoring point measurement

Setting up automatic measurement markers at a monitoring station can be an alternative method for manual field surveys. The control points can be set up in an area without displacement or even distributed based on error analysis. Monitoring stations can be measured by triangle trilateral intersection using a total station theodolite (TST). These control points can be used in photogrammetry to adjust the model scale and coordinate transformation. Some of the control points can be used as checkpoints to verify the overall measurement results. The difference between a control point and a checkpoint depends on whether the SfM-MVS uses these points as a constraint condition. Our system uses control points and checkpoints as monitoring points to determine whether displacement occurs.

3.3 Monitoring data analysis

3.3.1 Error analysis

In the process of 3D reconstruction, control points are used as a reference in converting the model from relative coordinates to absolute coordinates. Therefore, it is usually assumed that

Preprints (www.preprints.org) | NOT PEER-REVIEWED | Posted: 4 April 2018 doi:10.20944/preprints201804.0043.v1

control points should be positioned where change is thought least likely within the monitored area and, as a result, the calculated checkpoints can be expressed as absolute displacement. Table 1a shows the control points in an SfM-MVS system, and the magnitude of the error in the original data calculated from the control points and checkpoints. Table 1b shows a displacement of 20 mm (highlighted in red) for the simulated checkpoint, which will be directly displayed in the error and RMSE of the absolute displacement. However, such a hypothesis cannot be fully applicable because, in reality, it is difficult to find a truly unchanging area to set control points. First, suppose the control point (target 1) also starts to displace by about 20 mm: the red text in Table 1c does not display absolute displacement, but a calculated relative displacement with an error. Now, suppose the displacement control points are all simulated at 20 mm: the displacement is not fully reflected in Table 1d (red text), and the RMSE increases from its original value of 1.980 mm to 8.686 mm. The above abrupt change can be a reference to provide early warning of instability.

Table 1. Simulation of the monitoring point changes of SfM-MVS

				Simulation changes					
Raw data(a)				**2 point of check point(b)**		**1 point of control point(c)**		**All point of control point(d)**	
Control Point		Check Point		Control	Check	Control	Check	Control	Check
# Label	Error	# Label	Error	Error		Error		Error	
target 1	4.607	target 3	4.043	4.568	22.231	7.416	3.246	1.464	5.502
target 2	2.428	target 4	3.181	2.381	3.165	5.832	1.340	11.818	5.954
target 5	3.704	target 7	3.649	3.547	3.527	1.758	3.276	13.144	12.572
target 6	2.783	target 8	6.906	2.594	6.656	3.506	5.674	20.271	13.067
target 9	3.272	target 10	5.816	3.314	22.969	4.408	4.702	20.156	12.451
RMSE	1.980		2.843	1.946	8.518	2.873	2.271	8.686	6.053

Red text is simulation changes points. Unit:mm

3.3.2 Surface monitoring (SM)

If there is a risk of potential displacement after a monitoring point has been calculated, additional surface difference analysis can be performed. Point-cloud display technology, based on WebGL technology, can be used to display point-cloud differences, and the most convenient program to use is Three.js as the core of Potree [22]. Existing point-cloud difference-analysis methods include Cloud-to-Cloud (C2C), Cloud-to-Mesh (C2M) and Multiscale-Model-to-Model-Cloud (M3C2). C2C is the simplest and fastest way to calculate point-cloud distances because it does not use point-cloud meshing or calculate surface normals, and the method of computing distance includes average distance, best-fitting plane orientation and Hausdorff distance [23]. C2M, one of the most common methods at present, calculates the distance between point clouds and reference 3D grids or theoretical models. This method is more suitable for flat surfaces because computing points are most consistent with reference grids [24,25]. The M3C2 method combines the following three key features [26]: it operates directly on point clouds without meshing or gridding; it computes the local distance between two point-clouds along the normal surface direction, which tracks 3D variations in surface orientation; for each distance measurement it estimates a confidence interval depending on point-cloud roughness and registration error. There are advantages and disadvantages to all three methods and, in this paper, M3C2 is used to calculate the differences between two-point clouds.

3.4 Feed back

Early warning notifications from the monitoring system can be combined with administrators' existing communication methods, such as SMS newsletter, smartphone push, mail letter and communication software notifications. Administrators can consult the monitoring data analysis to determine whether there may be an immediate risk and send personnel to check. The system can also be combined with related national notification systems, such as the 'Taiwan road early natural

Preprints (www.preprints.org) | NOT PEER-REVIEWED | Posted: 4 April 2018 doi:10.20944/preprints201804.0043.v1

disaster prevention systems' (TRENDS) [27], or combined with XML data structures to issue related early warning messages; joint notifications can be issued via the system.

4. Case study

4.1 Experimental area

The case study used road-slope monitoring as an example. The experimental site was located in Gushan District, Kaohsiung City, Taiwan (Figure 8a). The automatic photography equipment was set up at 10-m intervals, and in total four units were set up to form the IoT_APM. The resolution of the camera was 6000 x 4000 pix, the focal length was 16 mm and the distance from the subjest was about 11.5 m, which converts to a ground sampling distance (GSD) of about 3 mm/pix. In this study, we setup 16 monitoring points using 12-bit CTs with a center radius of 25 mm (Figure 8b). The overall diameter of the coding standard is about 175 mm 58 pix, which is much larger than the identifiable 9-10 pix, and uses the local coordinate system to measure the coordinates of each monitoring point with the TST. This experiment was assumed to be temporary so a follow-up experiment was conducted without considering issues such as camera system setup and power supply. A single-shot range of 0 to 180 degrees required photographs at 10-degree intervals using four cameras giving a total of 76 images, and the internet connection used 4G LTE transmission. In the future, if site continuity is required, the system could be mounted on street lights and connected to mains electricity and a fixed network to address power and network problems.

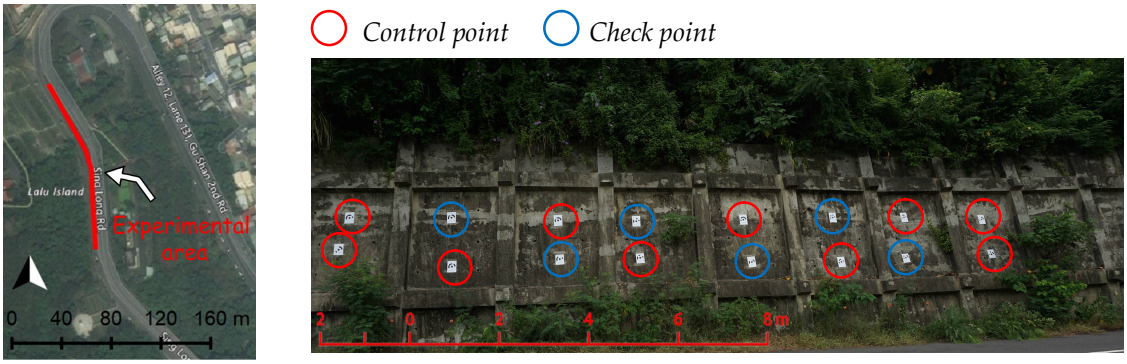

(a) (b)

Figure 8. (a)The setting of the experimental area. (b) The coded targets for the monitored points.

4.2 Error analysis

Error analysis was performed to verify the accuracy and reliability of the SfM-MVS method for use in stability monitoring. Between June and December 2014, SfM-MVS was used to conduct periodic manual inspections at the experimental site using various cameras, focal lengths, photography methods and automatic coding. Total Station measurement results were compared at the monitored points and the results show that the accuracy was within 0.5 pix [15]. Taking the automatic calculation result SfMID: 2000000021 of the system as an example, the maximum error of the monitored points (control and checkpoints) was 5.087 mm, the minimum was 0.011 mm, the total RMSE was 1.39 mm (about 0.463 pix), the control point RMSE was 2.934 mm and the monitored point RMSE was 1.651 mm. Each point is represented by the error vectors shown in Figure 9a and 9b. Additionally, the statistics on RMSE from 40 sets of monitoring data were analyzed to verify the stability of the method. The maximum RMSE of the control points was 3.81 mm, the minimum was 0.776 mm, the maximum RMSE of the monitored points was 3.695 mm and the minimum was 1.065 mm, as shown in Figure 9c. These results show that, when used with high precision and high stability, this method is suitable for monitoring.

Preprints (www.preprints.org) | NOT PEER-REVIEWED | Posted: 4 April 2018 doi:10.20944/preprints201804.0043.v1

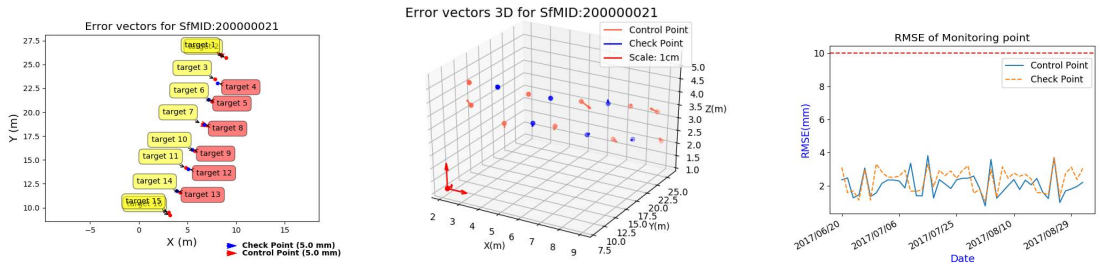

(a) (b) (c)

Figure 9. Monitored point error chart (a) Error vectors of monitored points (b) 3D Error vectors of monitored points and (c) 40 times RMSE of monitored points.

Road slopes require long-term, continuous monitoring to detect the initial signs of any instability. Therefore, to verify the feasibility of this method in road-slope monitoring, the following changes were made to the monitored points in the simulation. First, about 25-mm displacement was added to each control point in sequence, as shown in Figure 10. The upper-left 'raw data' show the original error at each monitoring point. Consequently, we assume that displacement is observed at one control point at a time; therefore, each subplot with the sub-title '1 to 10 points' shows the simulated displacement (error) values. 'Total RMSE' in the lower-left subplot shows the total RMSE calculated after control point displacement. The data show that the error increased from 4.28 mm to 18.405 mm when one control point was displaced and the total RMSE increased from 2.574 mm to 7.159 mm. After moving each control point sequentially, the error value of the displacement control point increased and the total RMSE also gradually increased to 20.172 mm.

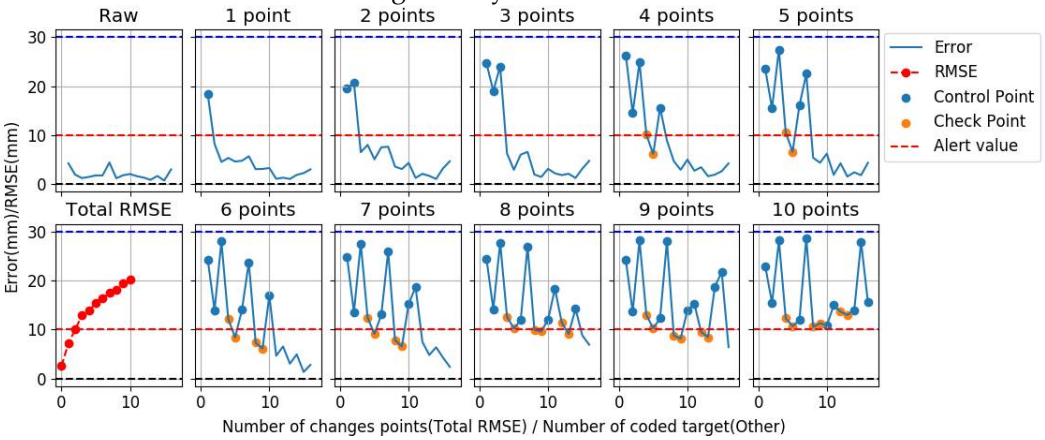

Figure 10. Simulation of control point displacement to calculate error and RMSE

The above method added displacement of a control point (with error) to the SfM-MVS calculation program, and the results show that it is not an absolute displacement but an overall minimum value. To verify that the control points with errors did not interfere with the SfM-MVS calculations, it was first assumed that each control point shifted by about 55 mm (the code target's outer circle distance), meaning that the calibration parameters of each camera were known to calculate the three-dimensional coordinates of each monitoring point. Finally, the Affine 3D parameters were calculated using the measured control points with the total least squares (TLS) and converted checkpoints. The results are shown in Table 2; (a) shows the differences in coordinates after Affine 3D conversion, (b) shows the control points with the error in coordinate differences calculated by PhotoScan, (c) shows the three-dimensional distances of the coordinate differences. The results show that: (1) the coordinates calculated by TLS and PhotoScan are close to each other (Table 2 c), and the results of TLS and PhotoScan should be based on the concept of minimizing the error of each point; (2) in the experiment example, the checkpoint is not displaced and, although some checkpoints in the calculation result show displacement, the main displacement still appears in the control point; (3) the control points in the SfM-MVS calculation program are used as the functions of coordinate transformation and scale control. The results show that errors in the control

Preprints (www.preprints.org) | NOT PEER-REVIEWED | Posted: 4 April 2018 doi:10.20944/preprints201804.0043.v1

points will not produce more errors in the calculation process. Therefore, this simulation experiment proves that the SfM-MVS method can display error points even when there is an error in the control point, and directly reflect the total RMSE. This feature for control point selection is convenient and can be used for early warning monitoring.

Table 2. Comparison of TLS-based 3D coordinate transfer and the PhotoScan method of simulating monitored point changes

Label	Diff. Of TLS (a)			Diff. Of PhotoScan (b)			Distance (c)		
	Δx	Δy	Δz	Δx	Δy	Δz	*Simulated moving*	*TLS*	*PhotoScan*
target 1*	-16.59	-62.83	4.76	-16.67	-62.94	4.76	59.18	65.16	65.28
target 2*	14.98	50.2	0.62	14.89	50.12	0.65	58.22	52.39	52.29
target 3*	15.21	52.23	-1.29	15.23	52.21	-1.31	55.55	54.41	54.40
target 4	1.06	-0.57	5.23	1.05	-0.55	5.24	0	5.37	5.37
target 5	0.14	3.15	0.56	0.2	3.19	0.53	0	3.20	3.24
target 6*	-17.6	-51.22	6.46	-17.55	-51.14	6.46	57.02	54.54	54.45
target 7*	14.85	63.55	0.37	14.94	63.65	0.35	57.5	65.26	65.38
target 8	2.16	6.24	3.45	2.24	6.36	3.43	0	7.45	7.57
target 9	2.57	13.41	0.96	2.65	13.52	0.95	0	13.69	13.81
target 10*	-14.77	-41.46	5.93	-14.68	-41.32	5.9	56.82	44.41	44.25
target 11*	-15.8	-40.85	0.54	-15.74	-40.7	0.54	60.17	43.80	43.64
target 12	4.23	15.48	4.7	4.29	15.59	4.67	0	16.72	16.83
target 13	7.19	20.12	0.15	7.19	20.12	0.17	0	21.37	21.37
target 14*	8.84	-16.52	-40.58	8.84	-16.48	-40.61	57.17	44.70	44.71
target 15*	19.89	77.35	20.89	19.82	77.24	20.93	57.96	82.55	82.44
target 16*	-8.99	-30.45	2.28	-9.06	-30.55	2.29	57.58	31.83	31.95
RMSE	**Control Point**		**25.791**			**25.785**	**57.73**	**55.59**	**55.56**
	Check Point							13.03	13.08

** Control point; Unit: mm*

4.3 Analysis of point-cloud difference

Generally, the accuracy of a dense point cloud is around two to three times the GSD. Suppose the point-cloud differences are calculated using the M3C2 method for two areas with no substantial changes and little disturbance (red area in Figure 11a), with an average of 0.07 mm and a standard deviation of 9.2 mm. Then remove the point cloud from one to three times the standard deviation (±9.2 mm~±27.6 mm) as shown in Figure 11b-11d. The experimental results show that one to three times the standard deviation accounts for 61% to 90% of the whole, and any more than three times the standard deviation is regarded as error, such as the planted or disturbed area in this example (Figure 11d). Therefore, taking a GSD of 3 mm as an example in this experiment, the standard deviation of point-cloud matching is about three times that of the GSD, and a standard deviation of more than three times can be regarded as a two-period difference area.

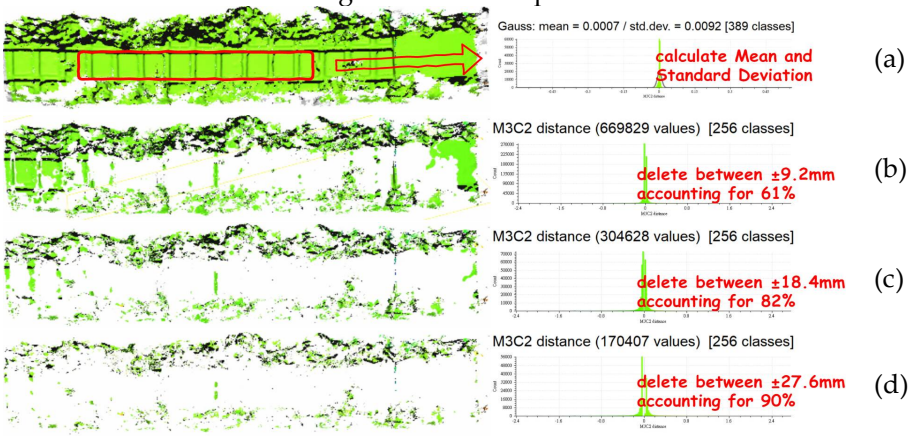

Figure 11. An example of dense point-cloud error with M3C2 distance (a) Original M3C2 distance (b) After deleting M3C2 distances between ±9 mm, (c) ±18 mm and (d) ±27 mm.

Preprints (www.preprints.org) | NOT PEER-REVIEWED | Posted: 4 April 2018 doi:10.20944/preprints201804.0043.v1

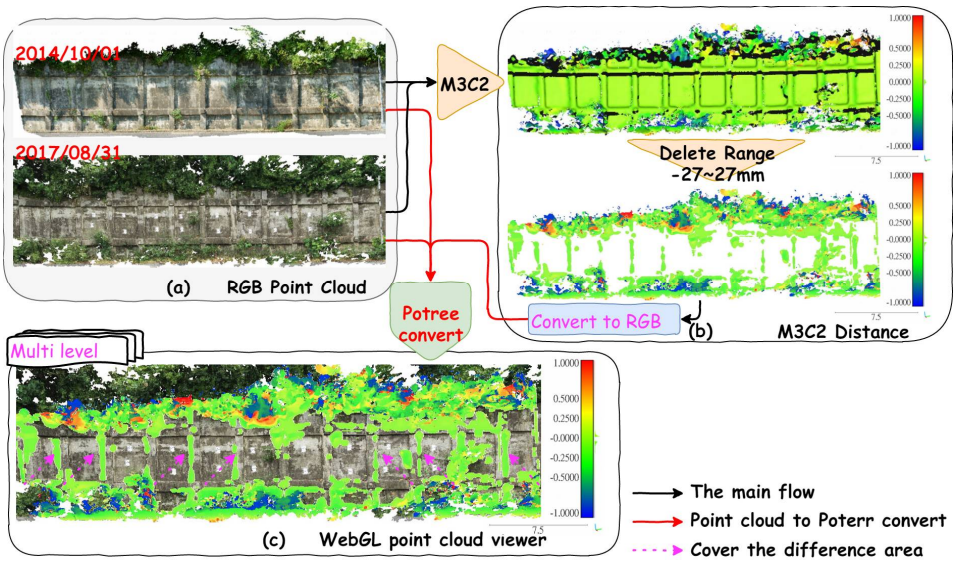

Figure 12. M3C2 distance to Potree viewer (a) Different color point cloud (b) M3C2 calculation and transfer and (c) Convert to Potree file format and display point cloud in WebGL.

Point-cloud-difference analysis provides a visual display of surface differences. In this study, dense point clouds were produced using PhotoScan and point-cloud-difference calculations (C2C or M3C2) were assessed using CloudCompare. Visual point-cloud difference display provides a real color point-cloud-nested M3C2 color-scale that uses the WebGL-based multi-scale octree to show a point cloud. The experimental M3C2 method for 2014/10/01 and 2017/08/31 data-point-cloud difference calculation (Figure 12a) first deleted data within three times the standard deviation and used shading to render point-cloud color (Figure 12b) Finally, the results were converted using Potree and displayed using WebGL to complete the point-cloud analysis.

After verification by TST in the experimental area, there was no substantial change in the main structure of the ground anchor slope protection area, which differed only where multiple plants were growing. However, as the shooting mode included rotating photography, numerous differences were caused by photographic masking (Figure 12c; magenta arrow). The use of rotation shooting by fixed cameras would alleviate this problem.

5. Conclusions

This study proposes a fully automatic road slope monitoring workflow, based on SfM-MVS photogrammetry, which provides full automation of photography, data transmission, calculation, error analysis, and surface difference analysis through a 3D displacement monitoring method. The above experiment showed that the automatic photography system, comprising the SBC with IoT architecture and digital cameras, can effectively solve the problem of automated photography and data transmission of a monitored site and effectively replace manual shooting. The simulation results showed that using SfM-MVS with TLS architecture effectively detected the relative displacement of monitored points. This feature solves the problem of traditional control points that have to be located outside the monitored area. The automatic calculation process design used in this study effectively solves the problems of photography measurement, calculation, analysis, and display, and makes this technology suitable for slope monitoring. Surface difference analysis calculates and removes data greater than three standard deviations from M3C2 and shows surface differences in a nested color point cloud. Continuous observation and verification can be applied to the monitoring of road slopes.

 doi:10.20944/preprints201804.0043.v1

Acknowledgments: This work has been supported by Harbor & Marine Technology Center, Institute of Transportation, Ministry of Transportation and Communications, R.O.C. The authors would also like to thank the reviewers for their time and their valuable comments.

Conflicts of Interest: The authors declare no conflict of interest.

References

1. Lane, S.; James, T.; Crowell, M. Application of digital photogrammetry to complex topography for geomorphological research. *The Photogrammetric Record* **2000**, *16*, 793-821.
2. Mallet, C.; Bretar, F. Full-waveform topographic lidar: State-of-the-art. *ISPRS Journal of photogrammetry and remote sensing* **2009**, *64*, 1-16.
3. Skarlatos, D.; Kiparissi, S. Comparison of laser scanning, photogrammetry and sfm-mvs pipeline applied in structures and artificial surfaces. *ISPRS annals of the photogrammetry, remote sensing and spatial information sciences* **2012**, *3*, 299-304.
4. Stumpf, A.; Malet, J.-P.; Allemand, P.; Pierrot-Deseilligny, M.; Skupinski, G. Ground-based multi-view photogrammetry for the monitoring of landslide deformation and erosion. *Geomorphology* **2015**, *231*, 130-145.
5. Javernick, L.; Brasington, J.; Caruso, B. Modeling the topography of shallow braided rivers using structure-from-motion photogrammetry. *Geomorphology* **2014**, *213*, 166-182.
6. Bigioi, P.; Susanu, G.; Corcoran, P.; Mocanu, I. Digital camera connectivity solutions using the picture transfer protocol (ptp). *IEEE Transactions on Consumer Electronics* **2002**, *48*, 417-427.
7. Osborne, R.; Van Zoest, A.; Robinson, A.; Fudge, B.; Srinivasan, M.; Fry, K. Media transfer protocol. Google Patents: 2010.
8. Hubert Figuière. Digital camera support for unix, linux and bsd. Available online: http://www.teaser.fr/~hfiguiere/linux/digicam.html (on 22 August 2017).
9. usb.org. Usb 2.0 specification(usb-port controller specification rev1.0 v1.2 final.Pdf). Available online: http://www.usb.org/developers/docs/usb20_docs/ (on 22 August 2017).
10. Ac power control by usb hub. Available online: http://www.gniibe.org/development/ac-power-control-by-USB-hub/ (on 22 August 2017).
11. Häming, K.; Peters, G. The structure-from-motion reconstruction pipeline–a survey with focus on short image sequences. *Kybernetika* **2010**, *46*, 926-937.
12. Seitz, S.M.; Curless, B.; Diebel, J.; Scharstein, D.; Szeliski, R. In *A comparison and evaluation of multi-view stereo reconstruction algorithms*, Computer vision and pattern recognition, 2006 IEEE Computer Society Conference on, 2006; IEEE: pp 519-528.
13. Furukawa, Y.; Ponce, J. Accurate, dense, and robust multiview stereopsis. *IEEE transactions on pattern analysis and machine intelligence* **2010**, *32*, 1362-1376.
14. Kazhdan, M.; Hoppe, H. Screened poisson surface reconstruction. *ACM Transactions on Graphics (TOG)* **2013**, *32*, 29.
15. Chiu, Y.F.; Lee, L.H.; Chang, T.R. *Automatic photographic monitoring system for the deformation of road slop*; MOTC-IOT-103-H1DB008; Harbor & Marine Technology Center: Taiwan, December, 2014.
16. Harwin, S.; Lucieer, A.; Osborn, J. The impact of the calibration method on the accuracy of point clouds derived using unmanned aerial vehicle multi-view stereopsis. *Remote Sensing* **2015**, *7*, 11933-11953.
17. Duane, C.B. Close-range camera calibration. *Photogrammetric Engineering* **1971**, *37(8)*, 855-866.

18. Maybank, S.J.; Faugeras, O.D. A theory of self-calibration of a moving camera. *International Journal of Computer Vision* **1992**, *8*, 123-151.
19. Van Den Heuvel, F.; Kroon, R.; Le Poole, R. Digital close-range photogrammetry using artificial targets. *International Archives of Photogrammetry and Remote Sensing* **1993**, *29*, 222-222.
20. Ganci, G.; Handley, H. Automation in videogrammetry. *International Archives of Photogrammetry and Remote Sensing* **1998**, *32*, 53-58.
21. Hattori, S.; Akimoto, K.; Fraser, C.; Ono, T.; Imoto, H. Design of coded targets and automated measurement procedures in industrial vision metrology. *International Archives of Photogrammetry and Remote Sensing* **2000**, *33*, 72-78.
22. Potree. Potree converter. Available online: https://github.com/potree/PotreeConverter (on 22 August 2017).
23. Girardeau-Montaut, D.; Roux, M.; Marc, R.; Thibault, G. Change detection on points cloud data acquired with a ground laser scanner. *International Archives of Photogrammetry, Remote Sensing and Spatial Information Sciences* **2005**, *36*, W19.
24. Monserrat, O.; Crosetto, M. Deformation measurement using terrestrial laser scanning data and least squares 3d surface matching. *ISPRS Journal of Photogrammetry and Remote Sensing* **2008**, *63*, 142-154.
25. Olsen, M.J.; Kuester, F.; Chang, B.J.; Hutchinson, T.C. Terrestrial laser scanning-based structural damage assessment. *Journal of Computing in Civil Engineering* **2009**, *24*, 264-272.
26. Lague, D.; Brodu, N.; Leroux, J. Accurate 3d comparison of complex topography with terrestrial laser scanner: Application to the rangitikei canyon (nz). *ISPRS Journal of Photogrammetry and Remote Sensing* **2013**, *82*, 10-26.
27. Chiu, C.K.; Yuan, C.M.; Wu, Y.W. *Trends maintenance and bridge assessment information integration*; MOTC-IOT-104-H1DC001; Harbor & Marine Technology Center: Taiwan, February, 2015; pp 3-1~3-11.